

RESEARCH ARTICLE

Non-invasive PET Imaging of PARP1 Expression in Glioblastoma Models

Brandon Carney,^{1,2} Giuseppe Carlucci,¹ Beatriz Salinas,¹ Valentina Di Gialleonardo,¹ Susanne Kossatz,¹ Axel Vansteene,¹ Valerie A. Longo,³ Alexander Bolaender,⁴ Gabriela Chiosis,⁴ Kayvan R. Keshari,^{1,5,6} Wolfgang A. Weber,^{1,5,6} Thomas Reiner^{1,6}

¹Department of Radiology, Memorial Sloan Kettering Cancer Center, New York City, NY, 10065, USA

²Ph.D. Program in Chemistry, The Graduate Center of the City University of New York, New York City, NY, 10018, USA

³Small-Animal Imaging Core Facility, Memorial Sloan Kettering Cancer Center, New York City, NY, 10065, USA

⁴Chemical Biology Program, Memorial Sloan Kettering Cancer Center, New York City, NY, 10065, USA

⁵Molecular Pharmacology Program, Memorial Sloan Kettering Cancer Center, New York City, NY, 10065, USA

⁶Weill Cornell Medical College, New York City, NY, 10065, USA

Abstract

Purpose: The current study presents [¹⁸F]PARPi as imaging agent for PARP1 expression.

Procedures: [¹⁸F]PARPi was generated by conjugating a 2*H*-phthalazin-1-one scaffold to 4-[¹⁸F]fluorobenzoic acid. Biochemical assays, optical *in vivo* competition, biodistribution analysis, positron emission tomography (PET)/X-ray computed tomography, and PET/magnetic resonance imaging studies were performed in subcutaneous and orthotopic mouse models of glioblastoma.

Results: [¹⁸F]PARPi shows suitable pharmacokinetic properties for brain tumor imaging (IC₅₀=2.8±1.1 nM; logP_{CHI}=2.15±0.41; plasma-free fraction=63.9±12.6 %) and accumulates selectively in orthotopic brain tumor tissue. Tracer accumulation in subcutaneous brain tumors was 1.82±0.21 %ID/g, whereas in healthy brain, the uptake was only 0.04±0.01 %ID/g.

Conclusions: [¹⁸F]PARPi is a selective PARP1 imaging agent that can be used to visualize glioblastoma in xenograft and orthotopic mouse models with high precision and good signal/noise ratios. It offers new opportunities to non-invasively image tumor growth and monitor interventions.

Key words: PARP1, Glioblastoma, PET, Orthotopic, Imaging

Introduction

Poly(ADP-ribose) polymerase 1 (PARP1)-targeted therapeutics have had a major impact on pharmaceutical research and development, and just recently, a therapeutic PARP1

inhibitor, Lynparza (olaparib, Astra-Zeneca), was approved for clinical use by the FDA [1–3]. The therapeutic interest in PARP1 is rooted in the unique role of the enzyme in the DNA damage repair cascade. PARP1 inhibitors inflict their cytotoxic potential by inhibiting certain cellular responses to DNA damage events, leading to cell death [1, 4]. The potential therapeutic impact of PARP1 as a clinical target is high, but the enzyme has also attracted attention as a target for imaging agents. This observation is based on the finding that PARP1 is highly overexpressed in various forms of cancer [5–11], and the degree of upregulation is linked to overall survival [7]. This implies that PARP1 is not only a

Brandon Carney and Giuseppe Carlucci contributed equally to this work. Electronic supplementary material The online version of this article (doi:10.1007/s11307-015-0904-y) contains supplementary material, which is available to authorized users.

Correspondence to: Thomas Reiner; e-mail: reinert@mskcc.org

Published online: 22 October 2015

therapeutic target but also a potentially valuable diagnostic or even prognostic biomarker.

Based on this data, we tested a fluorescent imaging agent, PARPi-FL [12, 13], for imaging of PARP1 expression *in vivo*. In mouse models of glioblastoma, we showed that PARPi-FL is metabolically stable, clears quickly from the circulation, and that its tumor uptake is closely correlated with PARP1 expression levels [14, 15]. Orthotopic brain tumors were successfully imaged *in vivo* due to (i) overexpression of PARP1 in glioblastoma, paired with (ii) low expression in healthy brain tissue; (iii) high cell permeability of the imaging agent; and (iv) strong retention in PARP1-expressing nuclei, along with rapid clearance from off-target tissues/cellular compartments.

While the fluorescent PARPi-FL will be of use as a preclinical imaging tool for quantifying PARP1 and might be used as an intraoperative probe, we became interested in creating a positron emission tomography (PET) active companion imaging agent for PARPi-FL. A radiolabeled PARP1 tracer might represent a robust platform for non-invasive PARP1 imaging and could ultimately provide insight into the biology of tumors before and after administration of treatment.

Inspired by our earlier designs [13–19] and the work of others [20], we synthesized [¹⁸F]PARPi, an F-18-labeled derivative of PARPi-FL. We determined the performance and basic binding parameters of [¹⁸F]PARPi in biochemical assays then showed that in optical imaging experiments, the radiolabeled tracer reaches its target on a cellular level, saturating PARP1 in the nuclei of glioblastoma cells. We determined the biodistribution of [¹⁸F]PARPi and showed in subcutaneous and orthotopic mouse models of glioblastoma that PARP1 expression can be visualized by PET with high signal/noise ratios.

Materials and Methods

A detailed description of the preparation of [¹⁸F]PARPi as well as of all *in vitro*, *in vivo*, and *ex vivo* experiments can be found in the Supplemental Data, together with additional supporting tables and figures. All animal experiments were done in accordance with protocols approved by the Institutional Animal Care and Use Committee of Memorial Sloan Kettering Cancer Center (MSKCC) and followed the National Institutes of Health guidelines for animal welfare.

Results

Chemistry and Radiochemistry

The molecular structure of [¹⁸F]PARPi is based on the previously tested and validated (2*H*)-phthalazin-1-one scaffold of the small molecule therapeutic olaparib [21]. Our tracer was obtained by conjugating a 4-[¹⁸F]fluorobenzoic acid group to the PARP1 targeting small molecule. Its cold reference compound, [¹⁹F]PARPi, was synthesized in a single synthetic step from 4-(4-fluoro-3-(piperazine-1-carbonyl)benzyl)phthalazin-1(2*H*)-one [21] and 4-fluorobenzoic acid, similar to coupling procedures applied

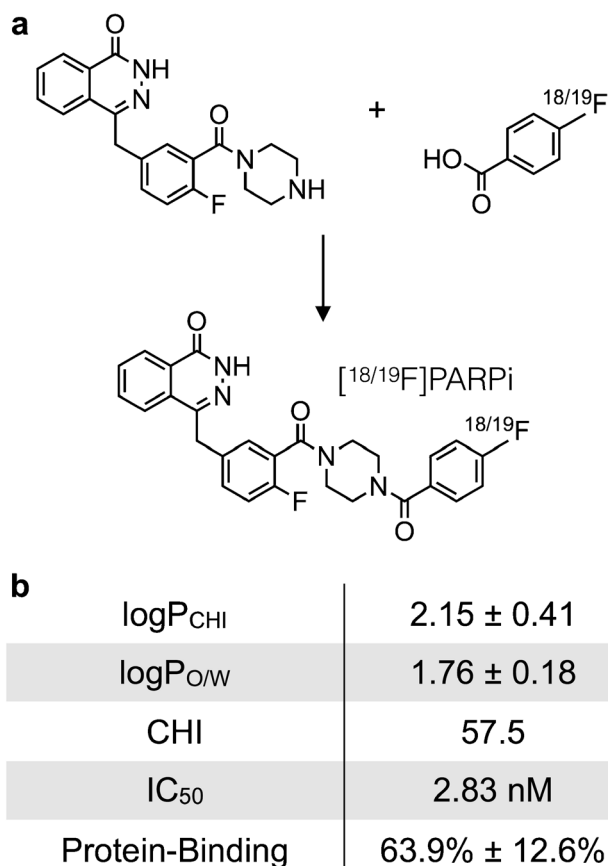


Fig. 1 Structure of [^{18/19}F]PARPi and biophysical properties. **a** 4-(4-Fluoro-3-(piperazine-1-carbonyl)benzyl)phthalazin-1(2*H*)-one (54.5 μmol) was conjugated with 4-fluorobenzoic acid (65.5 μmol) to yield the final [¹⁹F]PARPi. **b** Key pharmacokinetic properties of [¹⁹F]PARPi. logP_{CHI}=logP based on the chemical hydrophobicity index; logP_{O/W}=logP based on the octanol/water partition coefficient; CHI=chemical hydrophobicity index; IC₅₀=half maximal inhibitory concentration.

earlier [13] (Fig. 1a). [¹⁹F]PARPi was obtained with an isolated yield of 43 %, and its identity confirmed by ESI-MS, ESI-HRMS, and NMR spectroscopy (Fig. S1a–S1b).

The radiolabeled version of the PARP1-targeted tracer, [¹⁸F]PARPi, was synthesized in three consecutive synthetic transformations. Similar to the cold material, it was produced from the PARP1-targeted (2*H*)-phthalazin-1-one fragment. Its radiolabeled reaction partner 4-[¹⁸F]fluorobenzoic acid was obtained from ethyl 4-nitrobenzoate, which was added to dry K[¹⁸F]-K₂₂₂ and heated to 150 °C for 15 min to give ethyl 4-[¹⁸F]fluorobenzoate. The decay-corrected radiochemical yield (dcRCY) for this transformation was determined by HPLC and found to be 70 %. Then, the ethyl protective group was removed in the presence of sodium hydroxide to yield 4-[¹⁸F]fluorobenzoic acid (dcRCY>99 %). Analogous to the non-radioactive material, the radiolabeled 4-[¹⁸F]fluorobenzoic acid was coupled to the phthalazinone precursor (dcRCY=35 %). The total synthesis time from the start of synthesis to obtaining an injectable formulation was 90 min, and the overall

uncorrected radiochemical yield was 10 %, with a specific activity of 48 mCi/ μ mol (1.8 GBq/ μ mol, Fig. S2).

PARP1 Affinity, LogP, and Plasma Protein Binding of [19 F]PARPi

First, we determined the ability of our tracer to bind to PARP1 in a biochemical assay, analogous to methods we have previously described [22]. We found that the IC_{50} of [19 F]PARPi was 2.8 ± 1.1 nM (Fig. S1c), which is on par with the small molecule parent compound olaparib (5 nM, [21]). We calculated the $\log P_{CHI}$ of [19 F]PARPi from its chemical hydrophobicity index (CHI), a measure of HPLC retention time [23]. The CHI for [19 F]PARPi was 57.5, which translates to a $\log P_{CHI}$ of 2.15 ± 0.41 . This is concordant with measuring the octanol/water partition coefficient of [18 F]PARPi, where we determined the $\log P_{O/W}$ to be 1.76 ± 0.18 (Fig. 1b). The $\log P$ of [19 F]PARPi was higher than for olaparib ($CHI=34.1$, $\log P_{CHI}=0.8$), but both small molecules had comparable plasma protein binding (64 and 65 % for [19 F]PARPi and olaparib, respectively).

In vitro Characterization of [19 F]PARPi

We determined on a subcellular level whether [18 F]PARPi binds to the same target as its parent compound olaparib. To show this, we performed *in vitro* assays with the non-radioactive [19 F]PARPi, olaparib, and the fluorescent imaging agent PARPi-FL, which we have shown to be highly selective for PARP1 and suitable as a surrogate marker to infer the subcellular distribution of olaparib [18]. Labeling cells with PARPi-FL leads to strong nuclear fluorescence due to retention of the imaging agent by PARP1. In the presence of olaparib, the binding sites for PARPi-FL were occupied, and the observed fluorescence is reduced by 69.6 ± 22.3 % and 71.2 ± 20.0 % for U251 MG and U373 MG cells, respectively. Similarly, [19 F]PARPi was able to compete for the same binding sites as PARPi-FL, resulting in a reduction of fluorescence intensity in the nucleus by 80.0 ± 10.8 % and 78.8 ± 10.4 % for U251 MG and U373 MG cells, respectively (Fig. 2).

Blood Stability and Blood Half-Life of [18 F]PARPi

We estimated the *in vivo* stability of [18 F]PARPi by incubating the radiotracer in whole blood for up to 4 h. Over the given time period, no radioactive metabolites were observed, indicating excellent stability and potentially low bone uptake of the tracer for *in vivo* applications (Fig. S3). The blood half-life of [18 F]PARPi was determined in athymic nude mice, which received the tracer *via* tail vein injection. Analogous to other small molecules of this type [13, 14, 18], the agent was cleared rather quickly, with an alpha blood half-life of 1.27 min (85.51 %) and beta blood

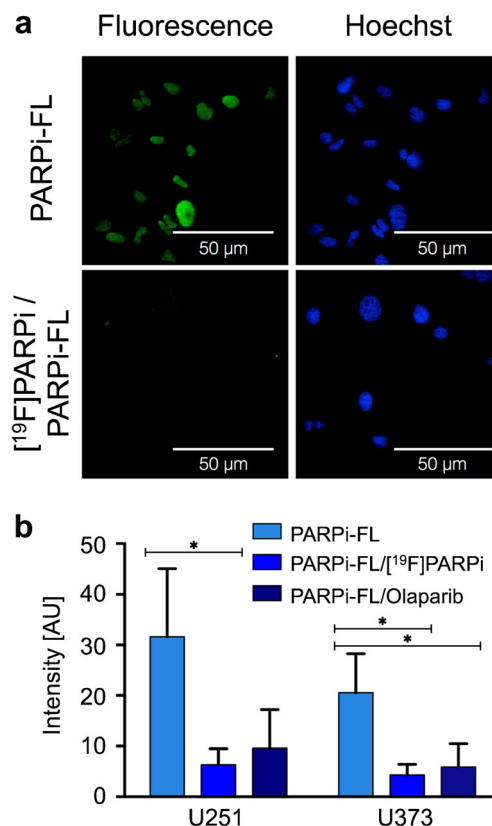


Fig. 2 Specificity of [19 F]PARPi uptake. U251 MG or U373 MG were incubated either alone with PARPi-FL (500 nM) or with PARPi-FL (500 nM) plus [19 F]PARPi (tenfold excess), or PARPi-FL (500 nM) plus olaparib (tenfold excess). [19 F]PARPi and olaparib compete for the same binding sites as PARPi-FL, resulting in a reduction of fluorescence intensity in case of specific binding. **a** Confocal microscopy of U251 MG cells after PARPi-FL or [19 F]PARPi /PARPi-FL injection. *Green* PARPi-FL signal, *blue* Hoechst nuclear stain. **b** Quantification of fluorescence intensity in cell nuclei in U251 MG and U373 MG cells after incubation with only PARPi-FL, [19 F]PARPi/PARPi-FL, or olaparib/PARPi-FL. *Error bars* are mean \pm standard deviation (SD). *P* values were calculated with Student's *t*-tests, unpaired; **P*<0.05.

half-life of 31.14 min (14.49 %), resulting in a weighted blood half-life of $t_{1/2}(\text{weighted})=5.6$ min (Fig. 3a).

Biodistribution

Biodistribution studies were performed in mice bearing subcutaneously injected U251 MG xenografts ($n=12$, Fig. 3b, c and Table S1). Tumor uptake at 2 h post-injection was 1.82 ± 0.21 %ID/g for mice receiving [18 F]PARPi (“unblocked”) and 0.23 ± 0.09 %ID/g for mice that were injected first with olaparib and 30 min later with [18 F]PARPi (“blocked”). Muscle uptake was 0.37 ± 0.09 %ID/g and 0.19 ± 0.08 %ID/g, while brain uptake was 0.04 ± 0.01 %ID/g and 0.04 ± 0.03 %ID/g for each group, respectively. The tumor-to-muscle ratio was 5.1 ± 0.9 , and

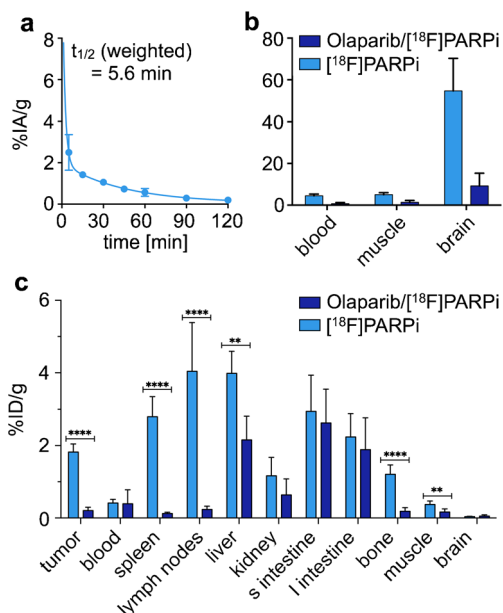


Fig. 3 $[^{18}\text{F}]\text{PARPi}$ *in vivo* pharmacokinetics. **a** *In vivo* blood half-life of $[^{18}\text{F}]\text{PARPi}$ ($n=3$). Blood was collected at different time points (5, 15, 30, 45, 60, 90, 120 min), weighted, and γ -counted. Results expressed as percent injected dose per gram (%ID/g). **b** Selected tumor-to-non-target-tissues ratio of $[^{18}\text{F}]\text{PARPi}$ ($n=12$) calculated from biodistribution data. **c** Biodistribution study in selected tissues. After injection of $[^{18}\text{F}]\text{PARPi}$ into mice with tumor xenografts, mice were euthanized at 2 h post-injection and radioactivity in organs was measured ($n=6/\text{group}$). Error bars are mean \pm SD. P values were calculated with Student's t -tests, unpaired; * $P < 0.05$; ** $P < 0.01$; *** $P < 0.001$; **** $P < 0.0001$.

the tumor-to-brain ratio was 54.9 ± 14.1 (Fig. 3b). A high uptake was also observed in the hepatobiliary system with liver uptake values of 3.98 ± 0.56 and 3.61 ± 2.04 %ID/g, small intestine uptake of 2.94 ± 0.91 and 2.35 ± 0.70 %ID/g, and large intestine uptake of 2.24 ± 0.59 and 1.73 ± 0.80 %ID/g for unblocked and blocked cohorts, respectively. We also found that lymph node and spleen uptake were high, with 2.80 ± 0.51 and 4.04 ± 1.23 %ID/g, respectively, and that their uptake was reduced after pre-injection of olaparib by 95 and 94 %, respectively (Fig. 3c). Highly selective uptake in these organs is based on their rather high PARP1 expression, shown in immunohistochemical stainings, which were obtained in non-tumor-bearing mice (Figs. S4–S5). Our biodistribution data was corroborated by PET/X-ray computed tomography (CT) imaging, with whole axial and coronal slices of subcutaneous tumor-bearing mice receiving only $[^{18}\text{F}]\text{PARPi}$ and both olaparib/ $[^{18}\text{F}]\text{PARPi}$ available in Supplemental Fig. S6.

Ex vivo Autoradiography

We used an orthotopic mouse model of U251 MG to determine the potential clinical impact of $[^{18}\text{F}]\text{PARPi}$ as a non-invasive PARP1 imaging tracer. U251 MG cells expressed PARP1 at much higher levels than healthy brain,

and orthotopic brain tumors had a high gradient in PARP1 expression (Fig. S7). In order to assess the alignment of $[^{18}\text{F}]\text{PARPi}$ retention and PARP1 expression on a microscopic level *in vivo*, tumor-bearing mice were injected with $[^{18}\text{F}]\text{PARPi}$ and autoradiography was performed (Fig. 4a). Using histology to localize the tumor regions of the brain, the autoradiographic analysis revealed significantly higher retention of $[^{18}\text{F}]\text{PARPi}$ inside orthotopic tumor tissue than in healthy surrounding brain (Fig. 4b, 46.66 ± 14.94 AU and 0.06 ± 0.02 AU for orthotopic tumor and surrounding brain, respectively). Similarly—and consistent with *in vitro* imaging—we found that pre-injection of olaparib and hence saturation of PARP1 binding sites lead to almost quantitative reduction of $[^{18}\text{F}]\text{PARPi}$ (99 %, 0.44 ± 0.41 AU and 0.03 ± 0.01 AU for orthotopic tumor and surrounding brain, respectively). The uptake of $[^{18}\text{F}]\text{PARPi}$ in orthotopic tumor tissue was distinctly higher than in muscle (Fig. 4b, c, 1.36 ± 0.21 AU and 1.50 ± 0.31 AU for muscle tissue in tumor-bearing and healthy mice, respectively).

PET/CT and PET/MRI Imaging in Orthotopic Mouse Models

We used both small-animal PET/CT and PET/magnetic resonance imaging (MRI) scanners to determine the accuracy and selectivity of non-invasive glioblastoma delineation with $[^{18}\text{F}]\text{PARPi}$. Figure 5a shows axial brain slices, obtained 120 min after radiotracer injection, of tumor-bearing animals that received either only $[^{18}\text{F}]\text{PARPi}$ or olaparib/ $[^{18}\text{F}]\text{PARPi}$. For animals receiving only $[^{18}\text{F}]\text{PARPi}$, the retained activity (2.15 ± 0.79 %ID/g) was eightfold higher than for animals that received both olaparib and $[^{18}\text{F}]\text{PARPi}$ (0.28 ± 0.01 %ID/g, Fig. 5b). Figure 5c shows representative 3D PET/CT reconstructions of orthotopic tumor-bearing mice that received $[^{18}\text{F}]\text{PARPi}$ or olaparib/ $[^{18}\text{F}]\text{PARPi}$. PET/MRI also confirmed uptake of $[^{18}\text{F}]\text{PARPi}$ in the tumor tissue, which was identified on T_1 -weighted post-contrast images (Fig. 6).

Discussion

The goal of this study was to establish an imaging tracer that can non-invasively detect PARP1 expression of malignant tumors. We showed that $[^{18}\text{F}]\text{PARPi}$, a PARP1-targeted small molecule, specifically binds to the DNA-repair enzyme PARP1 both *in vitro* and *in vivo*. Moreover, we tested the targeted accumulation of $[^{18}\text{F}]\text{PARPi}$ in orthotopic mouse models of glioblastoma and have shown with autoradiography PET/CT and PET/MRI that the tracer was retained inside of glioblastoma tissue, but not the surrounding healthy brain. This reflects the overexpression of PARP1 in orthotopic glioblastoma models (Fig. S7), which is consistent with our earlier findings [14, 15] and analogous to the human situation [9].

For the synthesis of $[^{18}\text{F}]\text{PARPi}$, we replaced the cyclopropane group from the PARP1-targeted (2*H*)-

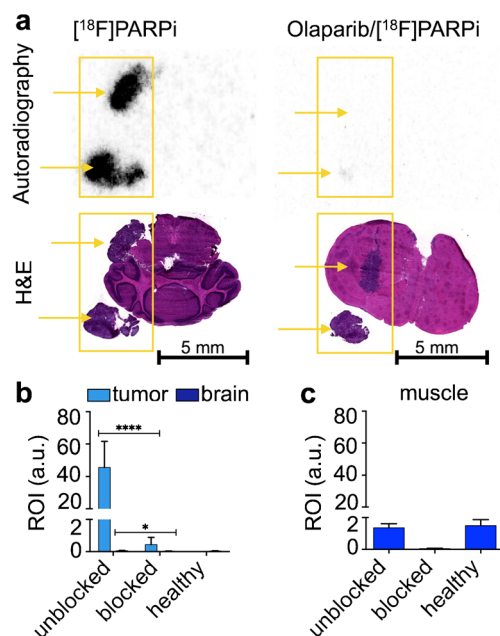


Fig. 4 $[^{18}\text{F}]\text{PARPi}$ localization in orthotopic U251 MG tumor-bearing mouse brain. **a** Autoradiography and H&E staining of U251 MG tumor-bearing brain sections of animals injected with $[^{18}\text{F}]\text{PARPi}$ or olaparib/ $[^{18}\text{F}]\text{PARPi}$. Yellow arrows indicate location of tumor tissue. Quantification of activity on autoradiographic sections in **b** orthotopic U251 MG tumors and mouse brain and **c** muscle of tumor-bearing mice that were unblocked and blocked, as well as unblocked healthy mice ($n=6$). Error bars are mean \pm SD. P values were calculated with Student's t -tests, unpaired; * $P<0.05$; ** $P<0.01$; *** $P<0.001$; **** $P<0.0001$.

phthalazin-1-one scaffold and with a 4- $[^{18}\text{F}]\text{fluorobenzene}$ to yield the target molecule, a strong binder of PARP1 (2.8 ± 1.1 nM). The radiochemical synthesis was straightforward, highly reproducible (Fig. S2), and produced the tracer in excellent yield (10 %, overall uncorrected radiochemical yield), radiochemical/chemical purity (>99 %), and specific activity (48 mCi/ μmol). Similar to what was already described by other groups [24, 25], the first two steps produced 4- $[^{18}\text{F}]\text{fluorobenzoic acid}$ in high yield. These steps were followed by efficient conjugation to the phthalazinone precursor in the presence of HBTU.

$[^{18}\text{F}]\text{PARPi}$ was rapidly washed out from most organs, resulting in a remarkable tumor-to-normal tissue contrast (Fig. 5) at 2 h post-injection for subcutaneous and orthotopic tumors. The tumor uptake of $[^{18}\text{F}]\text{PARPi}$ at 2 h was 2.2 ± 0.8 %ID/g and 1.82 ± 0.21 %ID/g for orthotopic and subcutaneous U251 MG xenografts, respectively, and higher than that of other PARP1 targeting molecules of this type [14, 19]. Moreover, 2 h post-injection, low activity concentrations were observed in most organs except for the gastrointestinal tract due to the rapid clearance from the blood and subsequent hepatobiliary excretion of the tracer (liver, 3.98 ± 0.56 %ID/g; small intestines, 2.94 ± 0.91 %ID/g; large intestines, 2.24 ± 0.59 %ID/g). This is analogous to

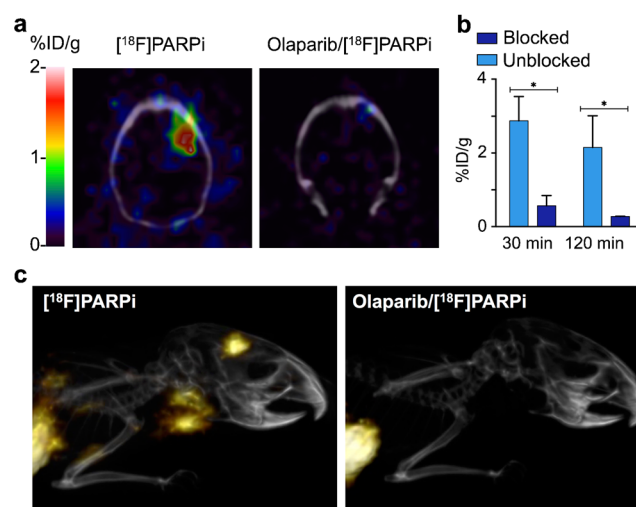


Fig. 5 *In vivo* whole body PET/CT imaging of $[^{18}\text{F}]\text{PARPi}$ in orthotopic brain tumor-bearing mice. **a** Fused PET/CT coronal images of a brain orthotopic U251 MG tumor-bearing mouse acquired at 2 h post-injection of $[^{18}\text{F}]\text{PARPi}$ (left) or the blocking agent olaparib (500-fold excess) followed by $[^{18}\text{F}]\text{PARPi}$ (right). **b** PET quantification of U251 MG tumors from images acquired at 30 min and 2 h post-injection ($n=10$). **c** Representative 3D PET/CT images of orthotopic U251 MG tumor-bearing mice after injection of $[^{18}\text{F}]\text{PARPi}$ (left) and after pre-injection (30 min before) of blocking agent and $[^{18}\text{F}]\text{PARPi}$ (500-fold excess olaparib) (right). Images were acquired at 2 h post-injection. Error bars are mean \pm SD. P values were calculated with Student's t -tests, unpaired; * $P<0.05$.

olaparib [26] and other PARP1-targeted molecules [14, 15, 27].

For PET/CT imaging in orthotopic U251 MG glioblastoma-bearing mice, imaging at 2 h rather than at 30 min post-injection yielded significantly higher tumor contrast by allowing the tracer to clear from the bloodstream

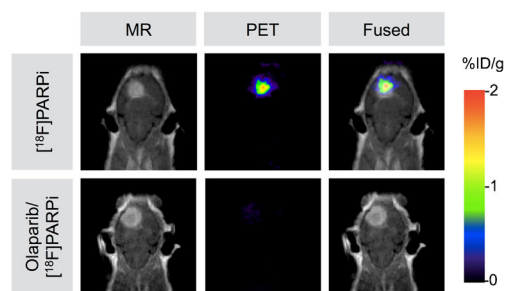


Fig. 6 *In vivo* whole body PET/MRI imaging of $[^{18}\text{F}]\text{PARPi}$ in orthotopic brain tumor-bearing mice. Coronal view of $[^{18}\text{F}]\text{PARPi}$ PET images, contrast-enhanced MRI, and fused PET/MRI of orthotopic U251 MG tumor-bearing mice. PET scans were acquired 2 h after injection of $[^{18}\text{F}]\text{PARPi}$ or olaparib/ $[^{18}\text{F}]\text{PARPi}$, and MRI scans were acquired 1 min after Magnevist injection. *Top row*: MRI, PET, and co-registered PET/MRI for a mouse receiving only $[^{18}\text{F}]\text{PARPi}$. *Bottom row*: MRI, PET, and co-registered PET/MRI for a mouse receiving $[^{18}\text{F}]\text{PARPi}$ after a 500-fold excess of olaparib.

and unspecific binding sites (Fig. 5 and Fig. S6, Table S1). PET quantification showed an uptake in the tumor of 2.88 ± 0.65 %ID/g at 0.5 h post-injection and 2.15 ± 0.28 %ID/g at 2 h post-injection.

Expanding on our *in vivo* imaging data, we confirmed the co-localization of [^{18}F]PARPi and tumor in PET/MRI studies and *ex vivo* autoradiography. In PET/MRI fusion images, accumulation in the tumor was co-aligned with the orthotopic tumor on MRI (Fig. 6, ~ 2 %ID/g). In mice receiving an injection of olaparib ahead of the radiotracer, the [^{18}F]PARPi tumor uptake was negligible (Figs. 5 and 6). This was also confirmed by *ex vivo* autoradiography (Fig. 4), in which a stark difference between tumor and non-targeted tissues (brain and muscle) was seen, which is likely the result of fast penetration and rapid washout kinetics of this class of imaging agents [18].

[^{18}F]PARPi combines good pharmacokinetic properties with remarkable *in vitro* and *in vivo* stability, evidenced by minimal defluorination. As result of the high lipophilicity of [^{18}F]PARPi, clearance mainly occurred *via* the hepatobiliary pathway, similar to olaparib and other PARP1-targeting molecules [14, 15, 27]. While imaging of glioblastoma with [^{18}F]PARPi in orthotopic mouse models was successful, it is a limitation of this model that the breakdown of the blood brain barrier can contribute to higher unspecific binding. Some of the tracer might have leaked out non-specifically into the tumor tissue due to this effect, contributing to the overall imaging signal. However, [^{18}F]PARPi uptake can be reduced significantly after injection of olaparib ($P < 0.0001$), which suggests that at least in areas where the blood brain barrier is disrupted, specific binding is observed. Retention of [^{18}F]PARPi in the lymph nodes and spleen was also blocked by injection of olaparib, and the uptake therefore likely reflects PARP1 expression in immune cells, which has been described in the literature [5] and is consistent with our histological findings (Figs. S4, S5).

Conclusion

The novel PET imaging agent [^{18}F]PARPi demonstrates an outstanding ability to non-invasively image PARP1 expression of gliomas and could have various applications in brain tumor research. Besides serving as a companion imaging agent for PARP1-targeting therapeutics, the agent could serve as a diagnostic for monitoring PARP1 expression before, during, and after treatment with cytotoxic agents. This could lead to new insights into the function of PARP1 during cellular DNA damage response. Furthermore, the biodistribution data indicates that the imaging of PARP1 expression is not only feasible for brain tumors but potentially also for lung and soft tissue tumors. This is of high clinical relevance, because PARP1 inhibitors are under clinical investigation in lung cancer, breast cancer, and sarcomas. These properties make [^{18}F]PARPi an excellent candidate for clinical translation.

Acknowledgments. The authors thank Dr. Jason S. Lewis and Dr. Edmund J. Keliher for helpful discussions, Dr. Christian Brand and Christopher P. Irwin for help with experiments and Leah Bassity for editing the manuscript. Technical services provided by the MSKCC Small-Animal Imaging Core Facility, supported in part by NIH Cancer Center Support Grant No 2 P30 CA008748-48, are gratefully acknowledged. NIH Shared Instrumentation Grant No 1S10 OD016207-01, which provided funding support for the purchase of the Inveon PET/CT, is gratefully acknowledged. The authors further thank the Molecular Cytology Core at Memorial Sloan Kettering Cancer Center (P30 CA008748). The authors thank the NIH (K25EB016673 for T.R.), the Brain Tumor Center of Memorial Sloan Kettering Cancer Center (for T.R.), the Center for Molecular Imaging and Nanotechnology (for T.R.), the Clinical and Translational Science Center (CTSC) at Weill Cornell Medical College (NIH/NCATS Grant TL1TR000459 for B.C.), the American-Italian Cancer Foundation (AICF) Post-Doctoral Research Fellowship (for G.C.), the German Research Foundation (for S.K.), as well as the National Science Foundation Integrative Graduate Education and Research Traineeship (IGERT 0965983 at Hunter College) for their generous support.

Author Contributions. The manuscript was written through contributions of all authors. All authors have given approval to the final version of the manuscript.

Compliance with Ethical Standards

Conflict of Interest The authors report no conflicts of interest.

References

- Rouleau M, Patel A, Hendzel MJ et al (2010) PARP inhibition: PARP1 and beyond. *Nat Rev Cancer* 10:293–301
- Gradwohl G, Menissier de Murcia JM et al (1990) The second zinc-finger domain of poly(ADP-ribose) polymerase determines specificity for single-stranded breaks in DNA. *Proc Natl Acad Sci U S A* 87:2990–2994
- Hassa PO, Hottiger MO (2008) The diverse biological roles of mammalian PARPs, a small but powerful family of poly-ADP-ribose polymerases. *Front Biosci* 13:3046–3082
- Yang KS, Kohler RH, Landon M et al (2015) Single cell resolution *in vivo* imaging of DNA damage following PARP inhibition. *Sci Rep* 5:10129
- Ossovskaya V, Koo IC, Kaldjian EP et al (2010) Upregulation of poly(ADP-ribose) polymerase-1 (PARP1) in triple-negative breast cancer and other primary human tumor types. *Genes Cancer* 1:812–821
- Bièche I, De Murcia G, Lidereau R (1996) Poly(ADP-ribose) polymerase gene expression status and genomic instability in human breast cancer. *Clin Cancer Res* 2:1163–1167
- Rojo F, Garcia-Parra J, Zazo S et al (2012) Nuclear PARP-1 protein overexpression is associated with poor overall survival in early breast cancer. *Ann Oncol* 23:1156–1164
- Alanazi M, Pathan AA, Arifeen Z et al (2013) Association between PARP-1 V762A polymorphism and breast cancer susceptibility in Saudi population. *PLoS One* 8, e85541
- Galia A, Calogero AE, Condorelli RA et al (2012) PARP-1 protein expression in glioblastoma multiforme. *Eur J Histochem EJH* 56
- Barton VN, Donson AM, Kleinschmidt-DeMasters BK et al (2009) PARP1 expression in pediatric central nervous system tumors. *Pediatr Blood Cancer* 53:1227–1230
- Staibano S, Pepe S, Lo Muzio L et al (2005) Poly(adenosine diphosphate-ribose) polymerase 1 expression in malignant melanomas from photoexposed areas of the head and neck region. *Hum Pathol* 36:724–731
- Thurber GM, Reiner T, Yang KS et al (2014) Effect of small-molecule modification on single-cell pharmacokinetics of PARP inhibitors. *Mol Cancer Ther* 13:986–995
- Reiner T, Lacy J, Keliher EJ et al (2012) Imaging therapeutic PARP inhibition *in vivo* through bioorthogonally developed companion imaging agents. *Neoplasia* 14:169–177
- Carlucci G, Carney B, Brand C et al (2015) Dual-modality optical/PET imaging of PARP1 in glioblastoma. *Mol Imaging Biol*. doi:10.1007/s11307-015-0858-0
- Irwin CP, Portorreal Y, Brand C et al (2014) PARPi-FL—a fluorescent PARP1 inhibitor for glioblastoma imaging. *Neoplasia* 16:432–440

B. Carney et al.: PARP1-Targeted Glioblastoma Imaging

- Keliher EJ, Klubnick JA, Reiner T et al (2014) Efficient acid-catalyzed (18) F/(19) F fluoride exchange of BODIPY dyes. *ChemMedChem* 9:1368–1373
- Keliher EJ, Reiner T, Turetsky A et al (2011) High-yielding, two-step 18F labeling strategy for 18F-PARP1 inhibitors. *ChemMedChem* 6:424–427
- Thurber GM, Yang KS, Reiner T et al (2013) Single-cell and subcellular pharmacokinetic imaging allows insight into drug action in vivo. *Nat Commun* 4:1504
- Reiner T, Keliher EJ, Earley S et al (2011) Synthesis and in vivo imaging of a 18F-labeled PARP1 inhibitor using a chemically orthogonal scavenger-assisted high-performance method. *Angew Chem Int Ed Engl* 50:1922–1925
- Zhou D, Chu W, Xu J et al (2014) Synthesis, [(1)(8)F] radiolabeling, and evaluation of poly(ADP-ribose) polymerase-1 (PARP-1) inhibitors for in vivo imaging of PARP-1 using positron emission tomography. *Bioorg Med Chem* 22:1700–1707
- Meneer KA, Adcock C, Boulter R et al (2008) 4-[3-(4-Cyclopropane-carbonylpiperazine-1-carbonyl)-4-fluorobenzyl]-2H-phthalazin-1-one: a novel bioavailable inhibitor of poly(ADP-ribose) polymerase-1. *J Med Chem* 51:6581–6591
- Reiner T, Earley S, Turetsky A, Weissleder R (2010) Bioorthogonal small-molecule ligands for PARP1 imaging in living cells. *ChemBiochem* 11:2374–2377
- Valko K, Bevan C, Reynolds D (1997) Chromatographic hydrophobicity index by fast-gradient RP-HPLC: a high-throughput alternative to log P/log D. *Anal Chem* 69:2022–2029
- Marik J, Sutcliffe JL (2007) Fully automated preparation of n.c.a. 4-[18F]fluorobenzoic acid and N-succinimidyl 4-[18F]fluorobenzoate using a Siemens/CTI chemistry process control unit (CPCU). *Appl Radiat Isot* 65:199–203
- Li X, Link JM, Stekhova S et al (2008) Site-specific labeling of annexin V with F-18 for apoptosis imaging. *Bioconjug Chem* 19:1684–1688
- Chen Y, Zhang L, Hao Q (2013) Olaparib: a promising PARP inhibitor in ovarian cancer therapy. *Arch Gynecol Obstet* 288:367–374
- Murai J, Huang SY, Renaud A et al (2014) Stereospecific PARP trapping by BMN 673 and comparison with olaparib and rucaparib. *Mol Cancer Ther* 13:433–443